APL Materials

RESEARCH ARTICLE | JANUARY 22 2024

Structural anisotropy in Sb thin films

Pradip Adhikari ; Anuradha Wijesinghe; Anjali Rathore ; Timothy Jinsoo Yoo ; Gyehyeon Kim; Sinchul Yeom ; Hyoung-Taek Lee ; Alessandro R. Mazza ; Changhee Sohn; Hyeong-Ryeol Park ; Mina Yoon ; Matthew Brahlek ; Honggyu Kim ; Joon Sue Lee

APL Mater. 12, 011116 (2024)
https://doi.org/10.1063/5.0159670

Structural anisotropy in Sb thin films

Cite as: APL Mater. 12, 011116 (2024); doi: 10.1063/5.0159670
Submitted: 25 May 2023 • Accepted: 8 December 2023 •
Published Online: 22 January 2024

Pradip Adhikari,[1] Anuradha Wijesinghe,[1] Anjali Rathore,[1] Timothy Jinsoo Yoo,[2] Gyehyeon Kim,[1,3] Sinchul Yeom,[4] Hyoung-Taek Lee,[1,3] Alessandro R. Mazza,[4] Changhee Sohn,[3] Hyeong-Ryeol Park,[3] Mina Yoon,[4] Matthew Brahlek,[4] Honggyu Kim,[2] and Joon Sue Lee[1,a)]

AFFILIATIONS

[1] Department of Physics and Astronomy, University of Tennessee, Knoxville, Tennessee 37996, USA
[2] Materials Science and Engineering, Herbert Wertheim College of Engineering, University of Florida, Gainesville, Florida 32611, USA
[3] Department of Physics, Ulsan National Institute of Science and Technology, Ulsan 44919, South Korea
[4] Materials Science and Technology Division, Oak Ridge National Laboratory, Oak Ridge, Tennessee 37831, USA

[a)] **Author to whom correspondence should be addressed:** jslee@utk.edu

ABSTRACT

Sb thin films have attracted wide interest due to their tunable band structure, topological phases, high electron mobility, and thermoelectric properties. We successfully grow epitaxial Sb thin films on a closely lattice-matched GaSb(001) surface by molecular beam epitaxy. We find a novel anisotropic directional dependence on their structural, morphological, and electronic properties. The origin of the anisotropic features is elucidated using first-principles density functional theory (DFT) calculations. The growth regime of crystalline and amorphous Sb thin films was determined by mapping the surface reconstruction phase diagram of the GaSb(001) surface under Sb_2 flux, with confirmation of structural characterizations. Crystalline Sb thin films show a rhombohedral crystal structure along the rhombohedral (211) surface orientation parallel to the cubic (001) surface orientation of the GaSb substrate. At this coherent interface, Sb atoms are aligned with the GaSb lattice along the [$\bar{1}$10] crystallographic direction but are not aligned well along the [110] crystallographic direction, which results in anisotropic features in reflection of high-energy electron diffraction patterns, misfit dislocation formation, surface morphology, and transport properties. Our DFT calculations show that the preferential orientation of the rhombohedral Sb (211) plane may originate from the GaSb surface, where Sb atoms align with the Ga and Sb atoms on the reconstructed surface. The formation energy calculations confirm the stability of the experimentally observed structures. Our results provide optimal film growth conditions for further studies of novel properties of $Bi_{1-x}Sb_x$ thin films with similar lattice parameters and an identical crystal structure, as well as functional heterostructures of them with III–V semiconductor layers along the (001) surface orientation, supported by a theoretical understanding of the anisotropic film orientation.

I. INTRODUCTION

Group-VA elemental thin films (phosphorus, arsenic, antimony, and bismuth) have gained significant attention in recent years due to rich and promising properties, such as high carrier mobilities, outstanding optical and thermodynamic responses, a tunable bandgap, and non-trivial topological phases.[1–4] Among the group-VA elements, Sb and Bi are relatively heavy elements with a strong spin–orbit coupling. Multiple topological phases in Sb and Bi thin films, including the quantum spin Hall insulator phase in the two-dimensional (2D) limit, the three-dimensional (3D) topological insulator (TI) phase, and the 3D higher-order TI phase, have been theoretically proposed, and some of the features have been experimentally demonstrated.[5–8] In general, electronic band structures with non-trivial topology can be modified by strain, electric and magnetic fields, and thickness. In Sb thin films, it is theoretically predicted that the quantum confinement effect opens up a bulk bandgap when the film thickness is less than 7.8 nm, where it enters the 3D TI regime. Going even below a certain thickness transforms the topological phase into the quantum spin Hall state because of the surface coupling effect.[5] Antimonene, the Sb analog of graphene, is a 2D hexagonal lattice of Sb atoms. In addition to the non-trivial topology of antimonene (quantum spin Hall state), remarkable properties including stability in the air, high elec-

tron mobility, and thermoelectric and ferroelectric properties have attracted wide interest.[9–12]

Precise control over the film thickness is critical to investigate the quantum confinement effect in Sb thin films, and molecular beam epitaxy (MBE) is advantageous for layer-by-layer construction of topological quantum materials.[13] By using MBE, Sb thin films have been synthesized on various substrates since the 1980s. Early studies of Sb films grown on GaAs(110), InP(110), and InP(001) focused on the use of Sb as a capping layer or a Schottky barrier.[14–17] Moreover, the deposition of Sb on direct band-gap semiconductors of InSb(111) and GaSb(111) has been investigated for the purpose of developing superlattices with indirect narrow gap/direct gap heterostructures.[18] Recent reports on epitaxial Sb mostly focus on the demonstration of ultrathin Sb films or antimonene layers for their novel 2D nature and topologically non-trivial properties. Due to the hexagonal lattice structure of antimonene, van der Waals 2D substrates such as graphene,[19] as well as the (111) surface orientation of copper,[20] have been used for MBE growth of Sb layers. The most common crystalline structure for group V elemental solids is the rhombohedral structure, thus also for Sb. Under an ultrahigh vacuum (UHV) environment, rhombohedral Sb(111) layers can be epitaxially grown on closely lattice-matched GaSb(111) with a hexagonal lattice arrangement.[18,21] However, on cubic (001) surface orientation, polycrystalline nucleation of Sb with rough surfaces was reported, with no success in epitaxial growth of Sb layers.[21]

In this work, we report wide-area Sb thin films coherently grown on cubic GaSb(001) surfaces by MBE. We carefully study the surface kinetics and crystalline phase of Sb on a closely lattice-matched cubic GaSb(001) surface under a UHV environment. We first delve into the surface kinetics of the GaSb(001) surface in the presence of Sb flux over a wide range of temperatures, from 450 °C down to room temperature, and find the nucleation conditions of Sb films. We employ *in situ* reflection high-energy electron diffraction (RHEED) patterns to observe surface reconstruction on the GaSb(001) surface, as well as abrupt changes occurring at the surface when Sb layers start to grow. We successfully grew crystalline Sb thin films coherent to the GaSb(001) atomic structures below 120 °C. The Sb structure turned out to be rhombohedral along the (211) surface orientation parallel to the cubic (001) surface orientation of the GaSb substrate, as confirmed by x-ray diffraction (XRD) and electron diffraction using transmission electron microscopy (TEM). We define the rhombohedral Sb lattice indexing in accordance with the rhombohedral unit cell. Our density functional theory (DFT) calculations establish a theoretical framework for understanding the early stage structural properties and atomic-level interactions that influence the orientation and phase preference of the growing Sb film. According to the DFT calculations, the anisotropic features in Sb thin films, which refer to the directional dependence of their structural and morphological properties, likely originate from the reconstruction of the GaSb surface that is formed prior to the Sb growth. No cubic phase of Sb was seen from any of the grown films, consistent with the unstable cubic phase of Sb at ambient conditions.[22] The observed Sb (211) planes are aligned to the GaSb(001) lattices along the [$\bar{1}$10] direction, whereas mismatched lattices are expected along the [110] direction. This anisotropic lattice matching of the rhombohedral Sb (211) and cubic GaSb(001) layers results in (1) spottiness of RHEED along the [110] crystallographic direction; (2) formation of misfit dislocations along the [$\bar{1}$10] direction; (3) elongated formation of Sb structures along the [$\bar{1}$10] direction, observed by scanning electron microscopy (SEM) and atomic force microscopy (AFM); and (4) anisotropic transport with relatively lower resistance along the [$\bar{1}$10] direction in comparison to the [110] direction. The observed anisotropic features can be significantly reduced by growing Sb films at lower temperatures. Our DFT calculations show that the Sb (211) layers with observed anisotropy are stable, due to the (1×3) surface reconstruction of the GaSb(001) surface. The successful demonstration of coherent, rhombohedral Sb thin films grown on cubic GaSb(001) substrates paves the way to embed crystalline Sb layers into well-developed and widely used cubic semiconductor substrates for fundamental studies of the topological nature of Sb thin films as well as for applications using the electronic, optical, and thermoelectric properties. This study can be further extended to studies of $Bi_{1-x}Sb_x$ thin films on lattice-matched cubic substrates. $Bi_{1-x}Sb_x$ has shown multiple topological phases, which have potential applications in spintronics and quantum computing.[23–25]

II. RESULTS AND DISCUSSION

A. Surface reconstruction and Sb film growth on GaSb(001) surface

To achieve optimal growth conditions for Sb thin films, a surface reconstruction phase diagram of the GaSb(001) surface was investigated. In an ultrahigh vacuum chamber, the native oxide on the GaSb(001) surface was thermally desorbed, as confirmed by the appearance of RHEED patterns in the presence of Sb_2 flux. A GaSb desorption temperature of 540 °C was used to calibrate the pyrometer. On the desorbed surface, a GaSb homoepitaxial buffer layer was grown at 450 °C, and streaky (1×3) RHEED patterns confirmed the smooth surface under Sb-rich conditions. The (1×3) RHEED patterns represent the (1×3) surface reconstruction of the GaSb surface, which has been extensively studied using various surface sensitive techniques, including RHEED, scanning tunneling microscopy, low-energy electron diffraction, reflectance anisotropy spectroscopy, x-ray photoelectron spectroscopy, Auger electron spectroscopy, and DFT calculations.[26–34]

To obtain the surface reconstruction phase diagram of GaSb in the presence of Sb_2 flux, the Sb_2 flux was kept constant, and the change in the RHEED patterns was tracked with the decrease in substrate temperature. When the RHEED patterns significantly changed with the deposition of the Sb layer at lower temperatures, the substrate temperature was raised above 400 °C until GaSb (1×3) RHEED patterns reappeared, and a thin GaSb layer was grown to obtain a smooth surface. This process was repeated with a change in the Sb_2 flux.

Figure 1 shows the phase diagram for the surface reconstruction of the GaSb(001) surface under Sb_2 flux in the substrate temperature range from 450 °C down to room temperature. The flux values are expressed in units of beam equivalent pressure (mbar) as measured by the beam flux monitor of a Bayard–Alpert ionization gauge. The temperature values above 270 °C were measured using a pyrometer focused on the sample, while the lower temperatures were from

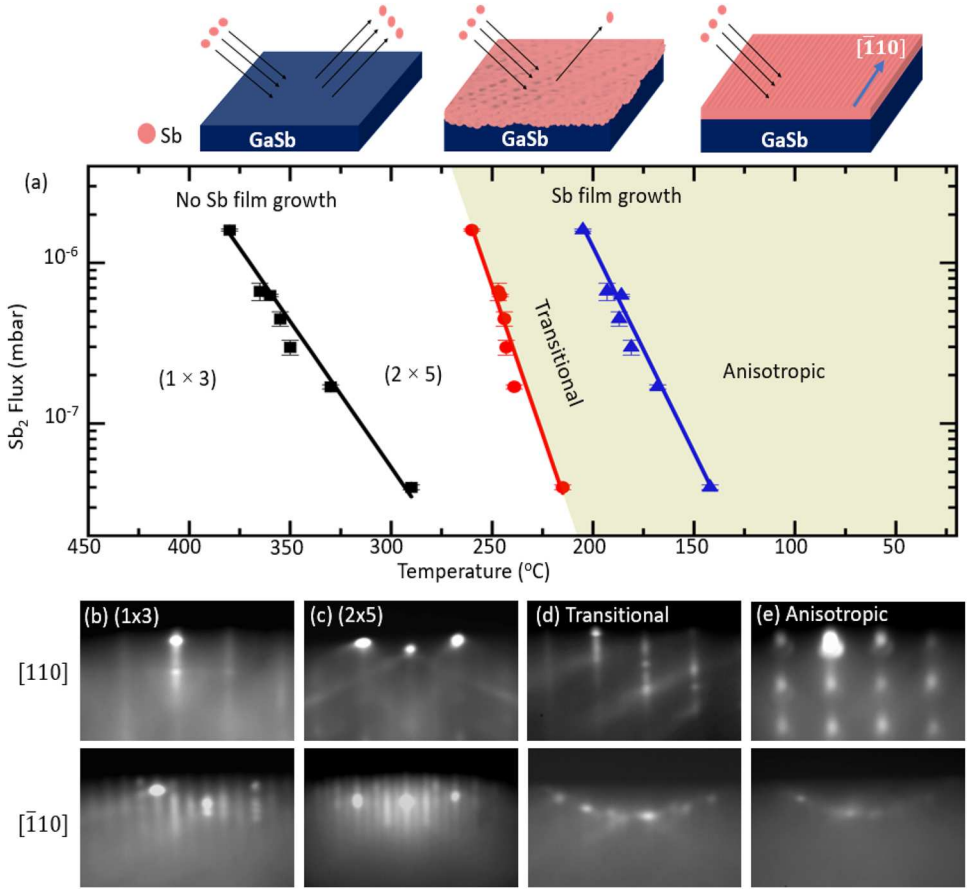

FIG. 1. (a) Surface reconstruction phase diagram for GaSb(001) in the presence of Sb_2 flux and Sb film growth illustration showing no growth, amorphous Sb with rough interface, and anisotropic crystalline Sb film with clean interface on GaSb(001) as growth temperature decreases. Representative RHEED images observed in (b) (1×3), (c) (2×5), (d) transitional, and (e) anisotropic RHEED regions. The shaded part indicates the region of Sb film growth. The error bars are the standard error of the mean from flux measurements on a beam flux monitor. The upper and lower rows show the RHEED images in the [110] direction and the [1̄10] direction, respectively.

a thermocouple attached to a manipulator holding the sample on a tungsten sample holder. The data points on the plots indicate transitions in the RHEED patterns. The $[(1 \times 3) \rightarrow (2 \times 5)]$ transition is the GaSb(001) surface reconstruction, consistent with previous reports,[28,29] indicating there is no Sb film grown on the surface. The RHEED pattern became blurry and dimmer between 200 and 250 °C, depending on the Sb_2 flux, indicating Sb atoms started to stick to the surface. Upon decreasing the substrate temperature, RHEED exhibited a sudden alteration, displaying distinctively spot-like patterns in the [110] direction and relatively indistinct but still streaky patterns in the [1̄10] direction. This implies that in the [110] direction, the electron beam detected three-dimensional nanostructures, while in the [1̄10] direction, it did not detect any significant three-dimensional features. This anisotropic spotty/streaky RHEED feature can be obtained with elongated 3D nanostructures on the surface, which is the case of the Sb thin films on the GaSb(001) surface, as confirmed by surface morphology characterizations. Sb thin films grown in the transitional and anisotropic RHEED regions were further characterized in the following sections.

B. Crystal structure of Sb thin films

To investigate the crystal structure of Sb thin films, two Sb films were prepared in the transitional and anisotropic RHEED regions based on the surface reconstruction phase diagram study. Two samples were grown at a manipulator temperature of 120 °C in the anisotropic RHEED region and at 250 °C in the transitional RHEED region, respectively, with identical Sb_2 flux of $(7.38 \pm 0.83) \times 10^{-7}$ mbar and growth time. While cooling down the substrate after GaSb buffer layer growth at 500 °C, the Sb_2 flux was closed below 400 °C to prevent any unattended Sb growth and reopened after the substrate reached the desired temperatures. High-resolution TEM (HRTEM) on a cross section of the sample grown at 120 °C shows the GaSb buffer layer, Sb film, and the protective Pt layer deposited by a focused ion beam [Fig. 2(a)].

The interface between Sb and GaSb is abrupt. Through selected area electron diffraction (SAED) analysis [Fig. 2(b)], the Sb film is determined to adopt the rhombohedral phase with a growth plane of $(211)_r$, where the subscript indicates the rhombohedral structure.

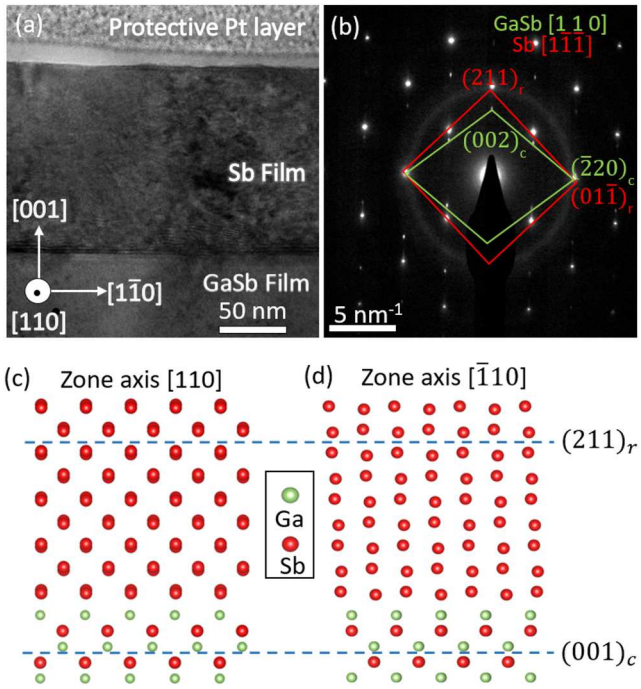

FIG. 2. (a) HRTEM image of the film stack for Sb film grown at 120 °C. (b) SAED pattern acquired at the interface between the GaSb buffer layer and Sb film. The diffraction spots for each structure are outlined in the red and green diamonds for Sb and GaSb, respectively. The $(001)_c$ growth plane of GaSb aligns with the $(211)_r$ growth plane of the Sb film. Illustrated crystal structure of rhombohedral Sb thin film on cubic GaSb layer, as shown in (c) along the $[110]_c$ zone axis and (d) along the $[\bar{1}10]_c$ zone axis.

The Sb growth plane of $(211)_r$ is parallel to the GaSb growth plane of $(001)_c$ of the cubic structure, which is later confirmed with the XRD measurement as well. Figures 2(c) and 2(d) illustrate the proposed growth orientation of the rhombohedral Sb on cubic GaSb according to these findings. Along the $[\bar{1}10]$ direction of GaSb, Sb atoms in the Sb film align well with Ga and Sb atoms in the GaSb layer, whereas the positions of the atoms in the two layers do not match along the [110] direction.

This lattice mismatch along the [110] direction is confirmed by high-angle annular dark-field scanning TEM (HAADF-STEM) on a cross section of the same Sb film along the $[\bar{1}10]_c$ zone axis (Fig. 3). The red planar streaks in the Sb film and GaSb buffer layer represent the $(011)_r$ and $(220)_c$ planes for the rhombohedral Sb and cubic GaSb structures, respectively [Fig. 3(a)]. The misfit at the interface of the two layers is correlated with misfit dislocations. Figure 3(c) shows the fast Fourier transform (FFT) of the HAADF-STEM image in Fig. 3(a). The selected spots in the two purple masks correspond to the $(011)_r$ and $(220)_c$ planes. An inverse FFT map using the spots reveals a more evident misfit between the Sb and GaSb planes [Fig. 3(d)]. The misfit dislocations, some of which are marked by yellow arrows in Fig. 3(d), at the interface between Sb and GaSb indicate that the Sb film is relaxed on the GaSb layer. In addition, in the Sb thin film with the expected rhombohedral lattice structure viewed along the $[0\bar{1}1]_r$ zone axis, low-angle grain boundaries (LAGBs) were observed with a small misorientation angle between the crystal lattices of the adjacent grains.

In contrast to the rhombohedral Sb thin film in the anisotropic RHEED region, the sample grown at 250 °C in the transitional RHEED region turns out to be amorphous, and the interface between Sb and GaSb is rougher than that of the sample grown at 120 °C (Fig. 4). A high-magnification HAADF-STEM image shows some crystallinity in the Sb film up to about 5 nm above the interface [Fig. 4(b)], but it is mainly amorphous beyond that region. It is likely that in the transitional RHEED region, Ga atoms from the GaSb layer diffuse into the Sb film, forming GaSb patches within the Sb film, as shown in Fig. 4(c). The orientations of the crystalline GaSb patches are different from each other, which is distinctive from the well-oriented single-crystalline GaSb layer below the interface. By using the same growth conditions (Sb flux and growth time), the thickness of the sample grown at 250 °C is around 25 nm, whereas the sample grown at 120 °C is much thicker (100 nm). This indicates that in the transitional RHEED region, Sb atoms are partially desorbed and partially deposited on the GaSb surface. No Sb peak was observed on the XRD of the sample grown at 250 °C, consistent with the amorphous nature observed by HAADF-STEM imaging. The formation of an amorphous film can be attributed to various factors related to thermal activation, mobility, kinetic competition, strain, mismatched crystal structures, and other material-specific properties. At high temperatures within the transitional RHEED region, Sb atoms gain kinetic energy and enhanced mobility, disrupting the crystalline order and resulting in the formation of an amorphous film. Mismatched crystalline structures between rhombohedral Sb and cubic GaSb, as well as the presence of nanometer-scale GaSb patches with different orientations, could contribute to the enhancement of amorphous structure formation. Notably, crystalline Sb(111) film was reported to form at 300 °C when grown on a single-crystalline rhombohedral GaSb(111) surface,[18] which contrasts with our findings.

To further achieve the optimal quality of the rhombohedral Sb thin films, four different samples expecting an equal thickness of ~50 nm were grown with a constant Sb flux of $(7.38 \pm 0.83) \times 10^{-7}$ mbar and manipulator temperatures (T_m) of 25, 60, 90, and 120 °C, respectively. The Sb film thickness was estimated from HRTEM measurements in Fig. 2(a) and further confirmed by x-ray reflectivity and AFM height profile measurements. (See the supplementary material, S2 and S3.). Before Sb film growth, following GaSb buffer layer growth at 500 °C with the (1×3) surface reconstruction, the Sb_2 flux was closed until the manipulator temperature reached the desired temperature. The (1×3) RHEED patterns of the GaSb surface were seen before the growth of the Sb films. (See the supplementary material, S1.) Figure 5(a) shows the XRD peaks of the samples, and all the films showed the crystalline nature of Sb. The peaks found at two values around 40.1° and 86.5° correspond with the Sb $(211)_r$ and Sb $(422)_r$ planes, respectively. The three tall peaks present in all the plots at 2θ angles of 29°, 61°, and 98° correspond with the peaks of GaSb$(002)_c$, $(004)_c$, and $(006)_c$. The XRD results confirm that Sb grows in the rhombohedral structure with the $(211)_r$ plane, which is parallel to the GaSb$(001)_c$ surface. The widths and heights of Sb XRD peaks vary depending on the growth temperatures. In particular, the height of the Sb $(422)_r$ peak decreases as the growth temperature increases. A rocking curve scan

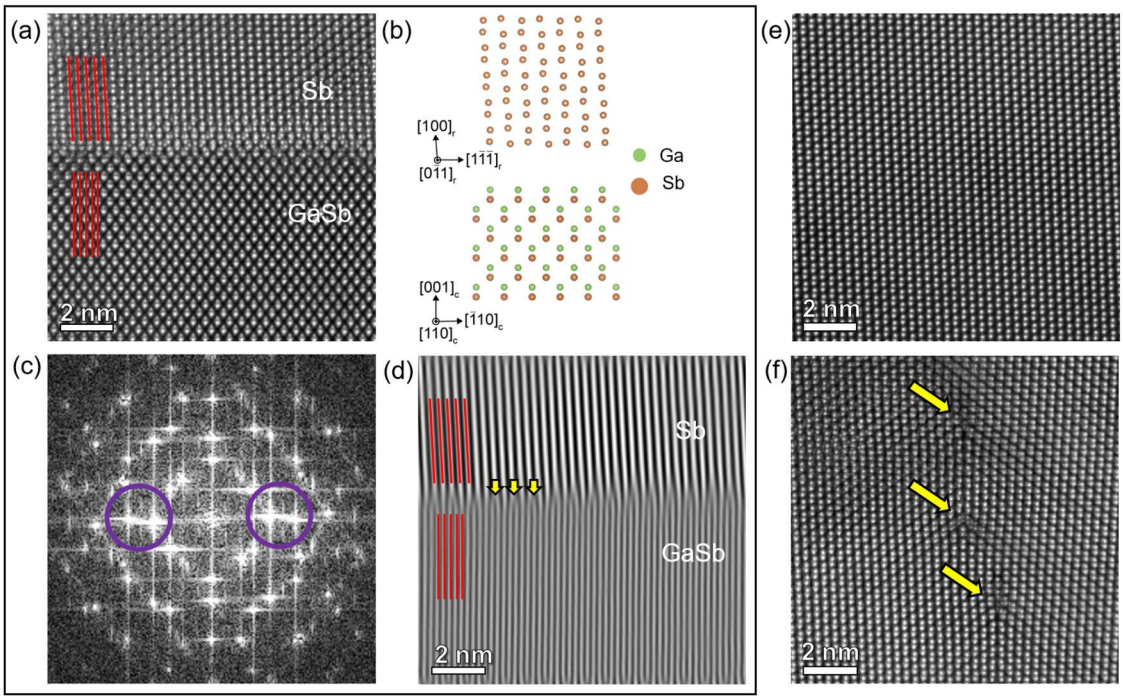

FIG. 3. (a) HAADF-STEM image of the interface between the Sb film and GaSb layer imaged along $[0\bar{1}1]_r$ and $[\bar{1}10]_c$. (b) Sb and GaSb crystal models for both zone axes projections. (c) FFT of the HAADF-STEM image in (a) with two masks in purple ever elected spots, corresponding to the $(011)_r$ and $(220)_c$ planes, for an inverse FFT analysis. (d) Inverse FFT pattern using the spots in the purple masks in (c). Some of the misfit dislocations are marked by yellow arrows. (e) HAADF-STEM image of the rhombohedral Sb film viewed along the $[0\bar{1}1]_r$ zone axis. (f) HAADF-STEM image of an array of dislocations marked with yellow arrows associated with LAGBs.

for each sample at $2\theta = 40.1^\circ$ with identical measurement conditions revealed a Gaussian-shaped rocking curve for all the samples. Consistent with the Sb XRD peak height variation, out of the four rocking curves, peaks from samples grown at 25 and 60 °C are significantly taller than those of samples grown at 90 and 120 °C, and Sb film grown at the highest temperature shows the shortest peak [Figs. 5(b) and 5(c)]. Full-width half maxima (FWHM) in Sb films grown at lower temperatures are narrower in comparison to those grown at higher temperatures, indicating higher film quality with fewer defects and curvature in films, consistent with the electron microscopy and RHEED results.

C. Anisotropic surface morphology

The surfaces of the samples grown at four different temperatures were scanned using SEM and AFM. SEM images in Figs. 6(a)–6(d) show line-like features along the $[\bar{1}10]$ direction in the samples grown at 60, 90, and 120 °C, while no prominent features were seen in the samples grown at 25 °C. The contrast of these lines appears to get stronger with increasing growth temperatures, which is consistent with the AFM results. The sample grown at 25 °C shows the smoothest surface with no clear tendency for directional structures, whereas slight elongation of nanostructures on the top surface starts to be seen in the sample grown at 60 °C [Figs. 6(e) and 6(f)]. Elongated Sb structures are more prominent in the samples with higher growth temperatures [Figs. 6(g) and 6(h)]. Surface roughness also increases with higher growth temperatures. The mean roughness values for the samples grown at 25, 60, 90, and 120 °C are 0.446, 0.479, 0.626, and 1.156 nm, respectively. The elongated Sb formation along the $[\bar{1}10]$ crystallographic direction can be attributed to the anisotropic lattice matching between the Sb $(211)_r$ and GaSb$(001)_c$ layers. This results in the formation of misfit dislocations preferentially along the $[1\bar{1}0]$ direction and associated LAGBs.

D. Anisotropic electrical transport

An anisotropy similar to that seen in surface morphology was also observed in electrical transport. The electrical resistance of the above four samples was measured in the square van der Pauw geometry at temperatures as low as 4 K (Fig. 7). Longitudinal resistance R_{yy} along the direction of the elongated Sb structures, the $[\bar{1}10]$ crystallographic direction, shows lower values compared to R_{xx}, which is in the [110] crystallographic direction. Due to the nature of the van der Pauw geometry, both R_{xx} and R_{yy} have contributions of electrical currents flowing in both [110] and $[\bar{1}10]$ directions. We assume R_{xx} has more contribution from the current along the [110] direction, whereas R_{yy} has more contribution from the current along the $[\bar{1}10]$ direction. The temperature range of interest is below 150 K, where charge carries in the GaSb buffer/substrate freeze, and its resistivity exponentially increases to be several orders of magnitude higher than that of Sb films. Samples grown at 25 and 60 °C show

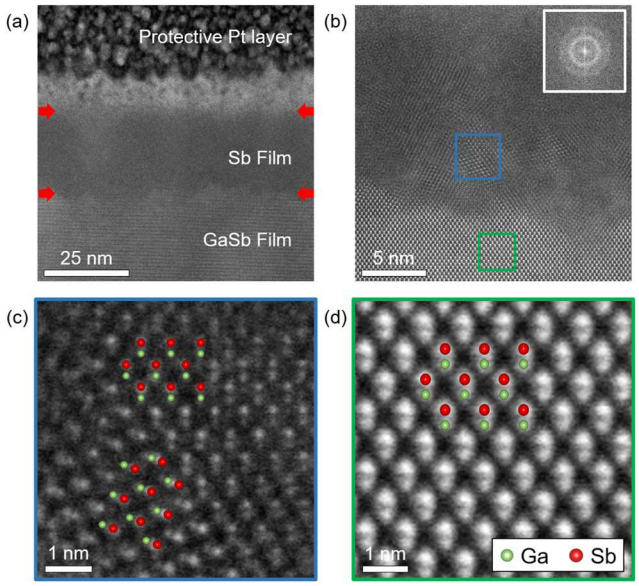

FIG. 4. (a) HAADF-STEM image of the film stack for Sb film grown at 250 °C. (b) High-magnification HAADF-STEM image near the interface between the Sb film and GaSb buffer layer, showing that the interface is rough. The top right inset is a fast Fourier transform (FFT) image of the Sb film away from the interface, showing ring patterns indicative of an amorphous structure. (c) Magnified image of one of several crystalline GaSb patches observed in the Sb film from the blue box in (b). (d) Magnified image of the GaSb buffer layer viewed along [110] from the green box in (b).

similar temperature dependence with metallic behaviors in both R_{xx} and R_{yy}, and the ratio of R_{xx} over R_{yy} is in the range of 2.1–2.5 at 4 K [Fig. 7(a)]. The longitudinal resistance of both crystallographic directions becomes more anisotropic as the substrate temperature increases. In samples grown at 90 and 120 °C, the ratio of R_{xx} over R_{yy} dramatically increases to 8 and 545, respectively, at 4 K. We attribute the anisotropic transport features of the Sb films to the anisotropic structure formation. The elongated, wire-like features along the [$\bar{1}$10] direction result in lower resistance in R_{yy}. In contrast, electrons moving along the [110] direction see more grain boundaries and curvature on the surface, which results in higher resistance and non-metallic temperature dependence in R_{xx}.

In addition, longitudinal (R_{xx} and R_{yy}) and transverse (R_{xy}) resistances were measured with respect to the perpendicular magnetic field (H) at different temperatures. Figures 7(b) and 7(c) show representative longitudinal and transverse curves for the sample grown at 25 °C. Measurements conducted on the other three samples revealed similar characteristics. The longitudinal resistance as a function of magnetic field (R vs H) displays a parabolic behavior in both R_{xx} and R_{yy} down to 4 K in all four samples. In single-crystal Sb, a near-quadratic (close to B^2) magnetoresistance was observed in the presence of a weak disorder.[35–37] This behavior was explained using a semiclassical framework for semimetals.[37] In Sb thin films, a transition from parabolic to linear magnetoresistance behavior with lowering the thickness was reported in Sb(111) thin films grown on GaSb(111)A substrates.[38] The 50-nm-thick Sb film examined in this work is in the 3D range with semimetallic band structures. The parabolic magnetoresistance behavior, shown in Fig. 7(b), is consistent with findings from semimetallic Sb single crystals and Sb(111) thin film studies in the thicker thickness regime.

The transverse resistance as a function of the magnetic field (R_{xy} vs H) exhibits a linear behavior. p-type carrier density of $n_{3D} = 9.82 \times 10^{20}$ cm^{-3} and hole mobility of 327.9 cm^2/V s were obtained for the sample grown at 25 °C. The high carrier density and the metallic temperature dependence of R_{xx} confirm the semimetallic nature of the Sb films. It is likely that one type of carrier (holes) dominates the transport mechanism, while the contribution from the other carrier (electrons) is negligible.

E. Anisotropic Sb film growth: surface reconstruction and formation energies

To gain further insight into the growth mechanisms of anisotropic Sb thin films, DFT calculations were performed

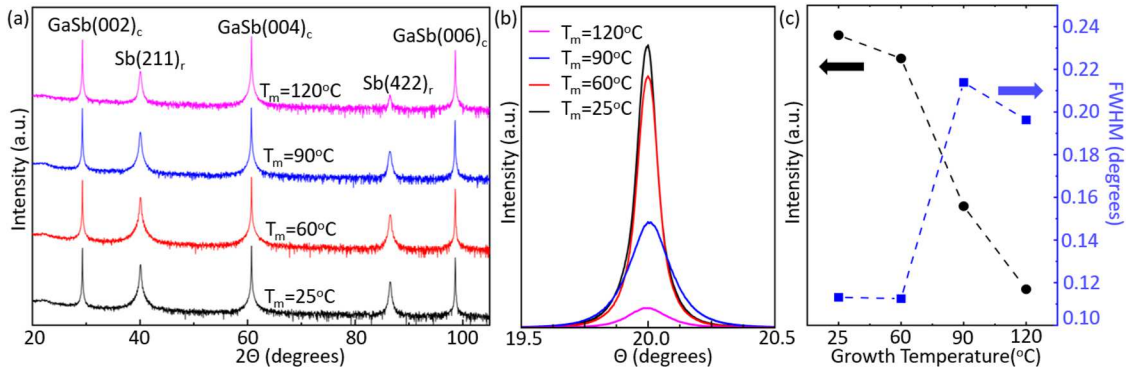

FIG. 5. (a) XRD for samples grown at 25, 60, 90, and 120 °C. The peaks appearing at 2θ values of 40.1° and 86.5° correspond to the Sb $(211)_r$ and $(422)_r$ planes, while the other peaks are emerging from the GaSb(001) substrate. (b) Rocking curves for the samples grown at 25, 60, 90, and 120 °C at a 2θ value of 40.1°. The peaks for samples grown at lower temperatures are taller and sharper, while samples grown at higher temperatures give broader and shorter peaks, as plotted in (c) Sb peak intensity (black circles) and FWHM (blue squares) of the samples grown at four different temperatures. Dashed lines are guides to the eye.

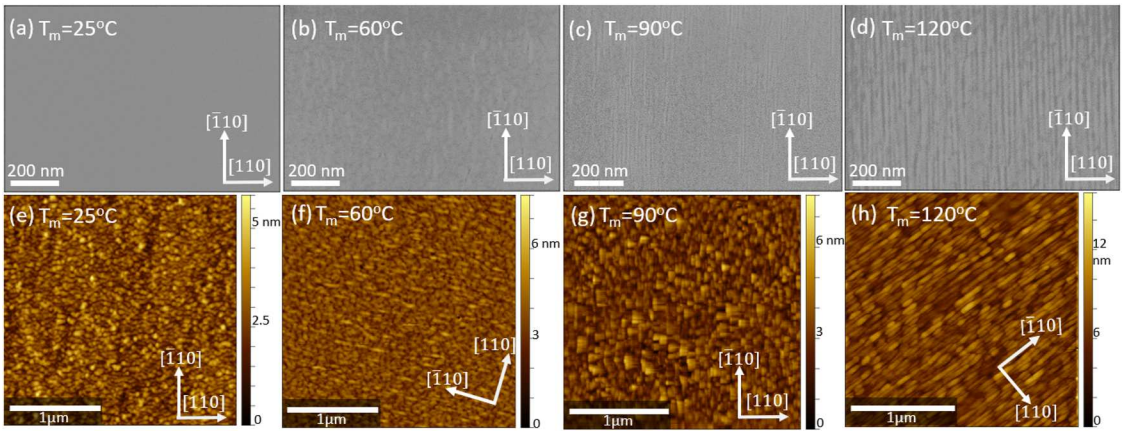

FIG. 6. (a)–(d) SEM and (e)–(h) AFM images for the samples grown at 25, 60, 90, and 120 °C. The roughness of the grown film increases with the growth temperature. Line-like features (elongated Sb structures) along the [$\bar{1}$10] direction are more distinct in the samples grown at higher temperatures.

using the FHI-aims code,[39–43] an all-electron code with localized numerical orbitals as the basis, tight basis sets, and the Perdew–Burke–Ernzerhof (PBE) exchange-correlation functional.[44] We employed the Hirshfeld scheme for the van der Waals interactions, which are important for the description of the layer interactions and also the interaction between the 2D film and the substrate.[45] The Broyden–Fletcher–Goldfarb–Shanno (BFGS)[46] algorithm was used for atomic relaxations with the condition that the maximum force component is less than 5×10^{-3} eV/Å.

We conducted a full relaxation of the GaSb unit cell structure and obtained a cubic lattice parameter of 6.125 Å. Using this structure, we generated a $3/\sqrt{2} \times 1/\sqrt{2} \times 4$ ($12.99 \times 4.330 \times 54.52$ Å^3, 35 Å vacuum) $(001)_c$ slab, which underwent structure relaxation with fixed lattice parameters. Subsequently, a (1×3) surface reconstructed $(001)_c$ structure emerged, as shown in Fig. 8(a), aligning with findings from previous experimental studies.[26,27] The 1×3 supercell (12.99×12.99 Å) of the surface-reconstructed GaSb substrate was employed as the substrate for placing a fully relaxed rhombohedral Sb slab—we found the supercell of the $2 \times 3 \times 2$ $(211)_r$ slab with 12.38×13.01 Å^2 matches well the lattice parameter of the substrate. The GaSb$(001)_c$ substrate has a cubic structure with 4-fold symmetry. The bulk crystal structure along the $[110]_c$ orientation is

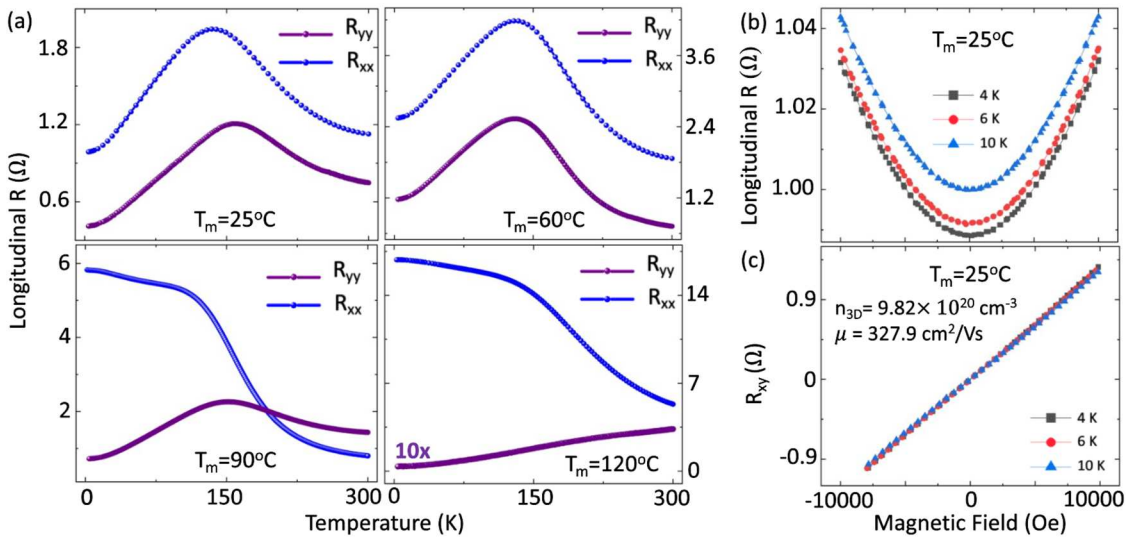

FIG. 7. (a) Resistance (R_{xx} and R_{yy}) vs temperature curves reveal anisotropic electrical properties in all four samples grown at 25, 60, 90, and 120 °C by using the square van der Pauw geometry in the [110] and [$\bar{1}$10] directions, respectively. (b) Longitudinal resistance (R_{xx}) vs magnetic field (H) shows parabolic behavior. (c) Transverse resistance (R_{xy}) vs magnetic field (H) shows a linear behavior at cryogenic temperatures.

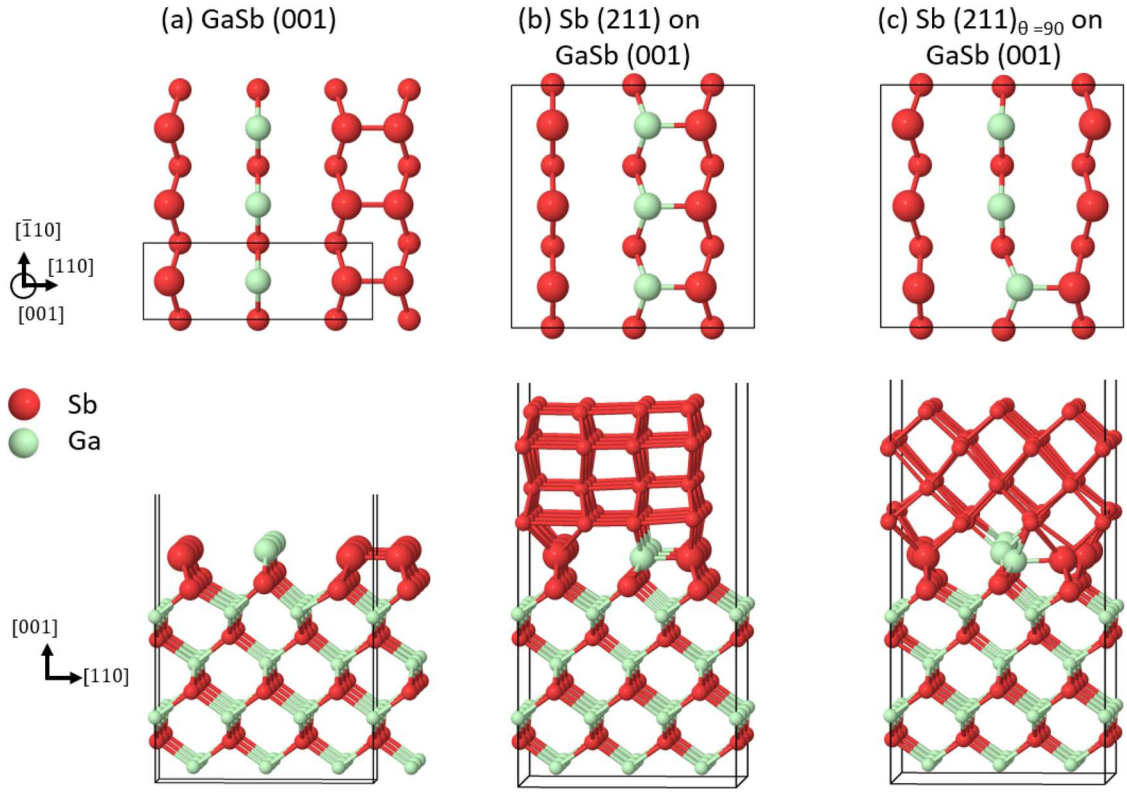

FIG. 8. First-principles modeling of Sb films on GaSb substrates. (a) Atomic structures of (1×3) reconstructed cubic GaSb(001). The (211) plane of the rhombohedral Sb film is well aligned with the (001) plane of the GaSb substrate in two different orientations shown in (b) and (c). The formation energy of the Sb (211) (b) on the reconstructed substrate (8.34 meV/Å^2) is found to be lower than that of (c) the 90°-rotated plane (10.9 meV/Å^2). The upper panel shows the atomic configurations of the GaSb at the interface with the 2D Sb.

identical to that along the $[\bar{1}10]_c$ orientation. The formation of elongated Sb structures along the $[\bar{1}10]_c$ orientation, but not along the $[110]_c$ orientation, on the GaSb$(001)_c$ substrate can be attributed to surface reconstruction of the GaSb substrate. The anisotropic Sb thin films were grown on the GaSb surface with a (1×3) surface reconstruction, as shown in Fig. 8(a). In this reconstructed GaSb surface, atoms on the top layers are distorted to minimize the surface free energy, leading to prominent features along the $[\bar{1}10]_c$ orientation. As a result, the Sb atoms are more likely to align with the Ga and Sb atoms on the reconstructed surface.

We considered two different cases for the incorporation of the $(211)_r$ slab: one in which the lowest Sb atoms of the Sb $(211)_r$ slab are aligned with the top Ga and Sb atoms of the GaSb substrate, and another with the $(211)_r$ slab rotated 90°. Both structures were fully relaxed, and the stable configurations are shown in Figs. 8(b) and 8(c). The rhombohedral Sb slabs of a few monolayers as a whole were incorporated without considering the Sb surface reconstruction during the growth. The formation energy of the 2D Sb was defined as $\Delta E = (E_{total} - N_{GaSb} \times E_{GaSb}^{3\times1} - N_{Sb} \times E_{Sb}^{bulk})/A$, where E_{total} is the total energy of the system consisting of 2D Sb on the GaSb substrate; $E_{GaSb}^{1\times3}$ is the energy per atom of the (1×3)-reconstructed GaSb; E_{Sb}^{bulk} is the energy per atom of the rhombohedral Sb bulk, a parent structure of the 2D film; N_{GaSb} and N_{Sb} are the number of atoms in the GaSb substrate and the Sb film; and A is the in-plane area of the supercell of the 2D Sb on GaSb. The formation energy of the Sb $(211)_r$ on the reconstructed substrate (8.34 meV/Å^2) is found to be lower than that of the 90°-rotated plane (10.9 meV/Å^2). This lower formation energy suggests that the observed Sb $(211)_r$ plane is energetically more favorable.

These calculations help to evaluate the energetics and structural stability of different configurations, which ultimately affect the growth behavior of the Sb films on GaSb$(001)_c$ substrates. This preferential growth of Sb structures along the $[\bar{1}10]_c$ orientation is further supported by the analysis of the formation energies. The DFT calculations reproduced the experimentally verified reconstruction of the substrate, which is the key to the growth of the Sb $(211)_r$ films with the preferred orientation.

III. CONCLUSIONS

In summary, we successfully mapped the growth regime of amorphous and crystalline Sb thin films on the GaSb(001) surface. We foun d that there is a transitional region between 250 and 150 °C where Sb atoms start to nucleate with the diffusion of Ga atoms to

form GaSb patches and then an amorphous Sb film, as confirmed by TEM. By avoiding Sb nucleation across the transitional region during the cooling process, crystalline Sb thin films were coherently grown on GaSb(001) below 120 °C. The crystal structure of the crystalline Sb thin films was found to be rhombohedral, with the Sb $(211)_r$ plane parallel to the cubic $GaSb(001)_c$ plane. At the interface, atoms of the rhombohedral Sb layer closely align with the GaSb lattice along the $[\bar{1}10]$ direction but not along the [110] direction, leading to the formation of misfit dislocations along the $[\bar{1}10]$ direction. This anisotropic lattice matching can be attributed to the (1×3) surface reconstruction of the GaSb(001) surface, as suggested by our DFT calculations. These calculations provide valuable insights into the formation energy and structural stability of different configurations, which in turn influence the growth behavior of Sb films on the $GaSb(001)_c$ substrates. The reduced formation energy of Sb $(211)_r$ on the reconstructed substrate determines the preferential orientation of the Sb plane. The formation of LAGBs with sequential misfit dislocations along the $[\bar{1}10]_c$ direction may further enhance the preferential growth of elongated Sb structures along the $[\bar{1}10]_c$ orientation. This leads to streaky/spotty RHEED patterns and anisotropic electronic transport. Such anisotropy is more prominent in samples grown at higher temperatures. The mean surface roughness of Sb thin film grown at room temperature is 2.5 times smaller than that of Sb thin film grown at 120 °C. The ratio of resistance along the [110] direction over the resistance along $[\bar{1}10]$ is two orders of magnitude higher for the Sb thin film grown at 120 °C in comparison to the one grown at room temperature. The successful demonstration of epitaxial Sb thin films on cubic GaSb(001) substrates opens a new avenue to embed rhombohedral Sb films on various cubic substrates, even with the fact that the cubic Sb phase is unstable. The systematic change in anisotropic features in the Sb thin films suggests optimal growth conditions for further studies and future applications using Sb thin films. For topological phases induced by the quantum confinement effect, smooth surfaces of Sb thin films with minimal anisotropy are preferred to achieve a uniform quantum confinement effect. For electrical and thermal transport, the crystallographic direction ($[\bar{1}10]$ vs [110]) needs to be considered according to the device applications.

SUPPLEMENTARY MATERIAL

See the supplementary material for additional RHEED images before and after Sb film growth at lower temperatures, x-ray reflectivity, and AFM height profile measurements to confirm the Sb film thickness.

ACKNOWLEDGMENTS

This work was supported by the Science Alliance at the University of Tennessee, Knoxville, through the Support for Affiliated Research Teams program, by the High-Potential Individuals Global Training Program (Task No. 2021-0-01580) through the Institute of Information and Communications Technology Planning & Evaluation (IITP) funded by the Republic of Korea Ministry of Science and ICT (MSIT) and by the U.S. Department of Energy (DOE), Office of Science, Basic Energy Sciences (BES), Materials Sciences and Engineering Division (MSED) (S.Y., M.B., and A.R.M.) and by the U.S. Department of Energy (DOE), Office of Science, National Quantum Information Science Research Centers, Quantum Science Center (M.Y.). This research used resources of the Oak Ridge Leadership Computing Facility (OLCF) and the Compute and Data Environment for Science (CADES) at the Oak Ridge National Laboratory, which are supported by the Office of Science of the U.S. Department of Energy under Contract No. DE-AC05-00OR22725 and of the National Energy Research Scientific Computing Center (NERSC), a U.S. Department of Energy Office of Science User Facility located at Lawrence Berkeley National Laboratory, operated under Contract No. DE-AC02-05CH11231 using NERSC Award No. BES-ERCAP0024568.

AUTHOR DECLARATIONS

Conflict of Interest

The authors have no conflicts to disclose.

Author Contributions

Pradip Adhikari: Data curation (lead); Formal analysis (lead); Project administration (supporting); Writing – original draft (lead); Writing – review & editing (lead). **Anuradha Wijesinghe**: Data curation (supporting); Formal analysis (supporting); Writing – original draft (supporting); Writing – review & editing (supporting). **Anjali Rathore**: Data curation (supporting); Formal analysis (supporting); Writing – original draft (supporting); Writing – review & editing (supporting). **Timothy Jinsoo Yoo**: Data curation (supporting); Formal analysis (supporting); Writing – original draft (supporting). **Gyehyeon Kim**: Data curation (equal); Formal analysis (equal); Writing – review & editing (equal). **Sinchul Yeom**: Data curation (supporting); Formal analysis (supporting); Writing – original draft (supporting); Writing – review & editing (supporting). **Hyoung-Taek Lee**: Data curation (supporting); Writing – review & editing (supporting). **Alessandro R. Mazza**: Data curation (supporting); Writing – review & editing (supporting). **Changhee Sohn**: Funding acquisition (supporting); Supervision (supporting); Writing – review & editing (supporting). **Hyeong-Ryeol Park**: Funding acquisition (supporting); Supervision (supporting); Writing – review & editing (supporting). **Mina Yoon**: Formal analysis (supporting); Investigation (supporting); Writing – original draft (supporting); Writing – review & editing (supporting). **Matthew Brahlek**: Data curation (supporting); Formal analysis (supporting); Writing – review & editing (supporting). **Honggyu Kim**: Data curation (supporting); Formal analysis (supporting); Supervision (supporting); Writing – original draft (supporting); Writing – review & editing (supporting). **Joon Sue Lee**: Conceptualization (equal); Formal analysis (equal); Funding acquisition (equal); Investigation (equal); Project administration (equal); Supervision (equal); Writing – original draft (equal); Writing – review & editing (equal).

DATA AVAILABILITY

The data that support the findings of this study are available from the corresponding author upon reasonable request.

REFERENCES

[1] S. Zhang, S. Guo, Z. Chen, Y. Wang, H. Gao, J. Gómez-Herrero, P. Ares, F. L. Zamora, Z. Zhu, and H. Zeng, Chem. Soc. Rev. **47**, 982 (2018).
[2] Z. Wu and J. Hao, npj 2D Mater. Appl. **4**, 4 (2020).
[3] R. Gui, H. Jin, Y. Sun, X. Jiang, and Z. Sun, J. Mater. Chem. A **7**, 25712 (2019).
[4] A. Zhao, H. Li, X. Hu, C. Wang, H. Zhang, J. Lu, S. Ruan, and Y.-J. Zeng, J. Phys. D: Appl. Phys. **53**, 293002 (2020).
[5] P. Zhang, Z. Liu, W. Duan, F. Liu, and J. Wu, Phys. Rev. B **85**, 201410 (2012).
[6] E. N. Lima and T. M. Schmidt, Phys. Rev. B **91**, 075432 (2015).
[7] S. Murakami, Phys. Rev. Lett. **97**, 236805 (2006).
[8] D. Wang, L. Chen, H. Liu, X. Wang, G. Cui, P. Zhang, D. Zhao, and S. Ji, Phys. Chem. Chem. Phys. **17**, 3577 (2015).
[9] P. Ares, J. J. Palacios, G. Abellán, J. Gómez-Herrero, and F. Zamora, Adv. Mater. **30**, 1703771 (2017).
[10] X. Wang, J. Song, and J. Qu, Angew. Chem., Int. Ed. **58**, 1574 (2019).
[11] S. Liu, T. Zhang, and S. Yang, "Antimonene: A potential 2D material," in *Monoelements* (John Wiley Sons, Ltd., 2020).
[12] C.-L. Xue and S.-C. Li, Jpn. J. Appl. Phys. **60**, SE0805 (2021).
[13] M. Brahlek, J. Lapano, and J. S. Lee, J. Appl. Phys. **128**, 210902 (2020).
[14] M. Dumas, M. Nouaoura, N. Bertru, L. Lassabatère, W. Chen, and A. Kahn, Surf. Sci. **262**, L91 (1992).
[15] S. A. Clark, J. W. Cairns, S. P. Wilks, R. H. Williams, A. D. Johnson, and C. R. Whitehouse, Surf. Sci. **336**, 193 (1995).
[16] H. Cheng, X. J. Zhang, and A. G. Milnes, Solid-State Electron. **27**, 1117 (1984).
[17] H. L. Kwok, Y. W. Lam, and S. P. Wong, Semicond. Sci. Technol. **2**, 288 (1987).
[18] C. K. Gaspe, S. Cairns, L. Lei, K. S. Wickramasinghe, T. D. Mishima, J. C. Keay, S. Q. Murphy, and M. B. Santos, J. Vac. Sci. Technol., B: Nanotechnol. Microelectron.: Mater., Process., Meas., Phenom. **31**, 03C129 (2013).
[19] X. Sun, Z. Lu, Y. Xiang, Y. Wang, J. Shi, G. C. Wang, M. A. Washington, and T. M. Lu, ACS Nano **12**, 6100 (2018).
[20] T. Niu, W. Zhou, D. Zhou, X. Hu, S. Zhang, K. Zhang, M. Zhou, H. Fuchs, and H. Zeng, Adv. Mater. **31**, 1902606 (2019).
[21] J. A. Dura, A. Vigliante, T. D. Golding, and S. C. Moss, J. Appl. Phys. **77**, 21 (1995).
[22] J. Donohue, *The Structures of the Elements* (Wiley, New York, 1974).
[23] M. Z. Hasan and C. L. Kane, Rev. Mod. Phys. **82**, 3045 (2010).
[24] N. H. D. Khang, Y. Ueda, and P. N. Hai, Nat. Mater. **17**, 808 (2018).
[25] A. R. Mellnik, J. S. Lee, A. Richardella, J. L. Grab, P. J. Mintun, M. H. Fischer, A. Vaezi, A. Manchon, E.-A. Kim, N. Samarth, and D. C. Ralph, Nature **511**, 449 (2014).
[26] G. E. Franklin, D. H. Rich, A. Samsavar, E. S. Hirschorn, F. M. Leibsle, T. Miller, and T. C. Chiang, Phys. Rev. B **41**, 12619 (1990).
[27] M. T. Sieger, T. Miller, and T. C. Chiang, Phys. Rev. B **52**, 8256 (1995).
[28] A. Bracker, M. Yang, B. Bennett, J. Culbertson, and W. Moore, J. Cryst. Growth **220**, 384 (2000).
[29] M. Nouaoura, F. W. Da Silva, N. Bertru, M. Rouanet, A. Tahraoui, W. Oueini, J. Bonnet, and L. Lassabatere, J. Cryst. Growth **172**, 37 (1997).
[30] A. Duzik and J. M. Millunchick, J. Appl. Phys. **116**, 023511 (2014).
[31] S. Hadenfeldt, C. Benndorf, A. Stricker, and M. Töwe, Surf. Sci. **352–354**, 295 (1996).
[32] C. Goletti, U. Resch-Esser, J. Foeller, N. Esser, W. Richter, B. Brar, and H. Kroemer, Surf. Sci. **352–354**, 771 (1996).
[33] F. Maeda, M. Sugiyama, and Y. Watanabe, Phys. Rev. B **62**, 1615 (2000).
[34] A. V. Vasev, M. A. Putyato, V. V. Preobrazhenskii, A. K. Bakarov, and A. I. Toropov, Semiconductors **52**, 664 (2018).
[35] M. C. Steele, Phys. Rev. **99**, 1751 (1955).
[36] N. B. Brandt, E. A. Svistova, and T. V. Gorskaya, Sov. Phys., Usp. **26**, 745 (1968), available at http://83.149.229.155/cgi-bin/e/index/e/26/4/p745?a=list.
[37] B. Fauqué, X. Yang, W. Tabis, M. Shen, Z. Zhu, C. Proust, Y. Fuseya, and K. Behnia, Phys. Rev. Mater. **2**, 114201 (2018).
[38] S. Cairns, N. Teasdale, J. Keay, C. K. Gaspe, K. S. Wickramasinghe, T. D. Mishima, M. B. Santos, and S. Q. Murphy, Phys. Rev. B **91**, 205317 (2015).
[39] V. Havu, V. Blum, P. Havu, and M. Scheffler, J. Comput. Phys. **228**, 8367 (2009).
[40] F. Knuth, C. Carbogno, V. Atalla, V. Blum, and M. Scheffler, Comput. Phys. Commun. **190**, 33 (2015).
[41] V. W. z. Yu, F. Corsetti, A. García, W. P. Huhn, M. Jacquelin, W. Jia, B. Lange, L. Lin, J. Lu, W. Mi, A. Seifitokaldani, Á. Vázquez-Mayagoitia, C. Yang, H. Yang, and V. Blum, Comput. Phys. Commun. **222**, 267 (2018).
[42] V. W. z. Yu, J. Moussa, P. Kůs, A. Marek, P. Messmer, M. Yoon, H. Lederer, and V. Blum, Comput. Phys. Commun. **262**, 107808 (2021).
[43] W. P. Huhn, B. Lange, V. W. z. Yu, M. Yoon, and V. Blum, Comput. Phys. Commun. **254**, 107314 (2020).
[44] J. P. Perdew, K. Burke, and M. Ernzerhof, Phys. Rev. Lett. **77**, 3865 (1996).
[45] A. Tkatchenko and M. Scheffler, Phys. Rev. Lett. **102**, 073005 (2009).
[46] J. Nocedal and S. J. Wright, *Numerical Optimization* (Springer, 1999).